UNIVERSIDAD DE CANTABRIA

Facultad de Ciencias

Departamento de Física Aplicada

Tesis Doctoral

SYNTHESIS, STRUCTURAL CHARACTERIZATION AND SPECTROSCOPIC STUDY OF NANOCRYSTALLINE AND MICROCRYSTALLINE MATERIALS

Rosa Martín Rodríguez

Santander, Noviembre de 2010

Conclusions

GGG and YAG nanoparticles co-doped with Tb^{3+} or Eu^{3+} and Yb^{3+} have been prepared by the sol-gel Pechini's method. The average size of the particles is around 30-40 nm, as shown by XRD and TEM measurements. Green and blue Tb^{3+} emission as well as red Eu^{3+} luminescence have been studied and identified. Excitation in the NIR region around 10250 cm^{-1} leads to strong Tb^{3+} and Eu^{3+} visible UC emission at RT. The experimental results and theoretical rate equations model confirm the cooperative sensitization as the UC mechanism responsible for the UC luminescence. The presence of Er^{3+} impurities and its consequent luminescence upon 10250 cm^{-1} excitation in Eu^{3+}-Yb^{3+} co-doped systems is not relevant for the Eu^{3+} UC emission.

5.3 Rare-earth and transition-metal ions co-doped systems

In the previous section, different UC systems involving combinations of RE ions have been studied. Opposite to f−f transitions in RE ions, d−d transitions of TM ions are much more sensitive to the local environment, and therefore, associated UC properties might be tuned by changing the crystal composition [45] or by applying hydrostatic pressure [46]. For instance, depending on the crystal-field strength, Mn^{2+} can emit from the blue-green to the deep red spectral region. In this sense, the combination of lanthanide and TM ions extends the UC luminescent tuning capability through changes in both energy resonances and emitting state energies.

The first demonstration of UC luminescence in TM-RE mixed systems was observed in Yb^{3+}-doped $CsMnCl_3$ and $RbMnCl_3$, and in Cr^{3+}-Yb^{3+} co-doped $Y_3Ga_5O_{12}$ at low temperatures [47], [48]. A GSA/ESA process between Mn^{2+}-Yb^{3+} dimer states was established as the main mechanism involved in the red UC luminescence in Yb^{3+}-doped $RbMnCl_3$ single-crystal [49]. This host incorporates trivalent impurities as Mn^{2+}-Yb^{3+} pairs with charge compensation vacancies. The use of manganese hosts ensures clustering since Yb^{3+} ions has always a Mn^{2+} ion as a near neighbor. The same model was proposed to explain both Mn^{2+} and Yb^{3+}-pairs UC emission in Yb^{3+}-doped $CsMnBr_3$

single crystals [50]. Evidence of GSA/ETU between Mn^{2+}-Yb^{3+} dimers was found in Yb^{3+}-doped $CsMnCl_3$ [19]. All these compounds showed UC luminescence only at low temperature. It is well known that concentrated TM compounds exhibit luminescence quenching as temperature increases. This phenomenon was explained by thermally activated excitation migration and subsequent transfer to non-radiative traps [51]. Therefore, the temperature-induced luminescence quenching is inherent to concentrated manganese systems, and occurs independently of the excitation way, either in the NIR or directly in the Mn^{2+} ions in the UV-visible region, although the quenching temperature is lower in the former case. Since the Mn^{2+}-Yb^{3+} UC systems studied up to now were only efficient at cryogenic temperatures, the combination of TM and RE ions has not been exploited for applications as UC luminescent materials.

Another difficulty related to the UC luminescence investigation involves finding suitable host lattices able to accommodate both Mn^{2+} and Yb^{3+} at well defined sites without charge compensation. Regarding this subject, micropowders of LMA co-doped with different Mn^{2+} and Yb^{3+} concentrations have been prepared in this work. As we will see, this host meets the impurities incorporation requirements. Since the as obtained powders can be milled in the planetary ball mill subsequently, this might be a good initial step to obtain LMA: Mn^{2+}, Yb^{3+} nanoparticles. The experimental results shown in this section allow to establish the UC mechanisms involved in Mn^{2+}-Yb^{3+} co-doped LMA, and determine the effect of doping concentrations on the UC efficiency.

5.3.1 Mn^{2+}, Yb^{3+} co-doped $LaMgAl_{11}O_{19}$

Synthesis and characterization

LMA crystallizes in the $PbFe_{12}O_{19}$ *magnetoplumbite*-type structure (hexagonal, $P6_3/mmc$ space group) [52]. It consists of spinel blocks separated by an intermediate layer containing three oxygen ions, one lanthanum and one aluminum per spinel block. Mg^{2+} ions are accommodated into the spinel blocks. LMA doped with Mn^{2+} is a well-known green phosphor which can be excited by vacuum UV radiation and used in plasma display panels [53]. In Mn^{2+}-Yb^{3+} co-doped LMA, Mn^{2+} ions occupy the tetrahedral Mg^{2+} sites whereas Yb^{3+} replaces La^{3+}.

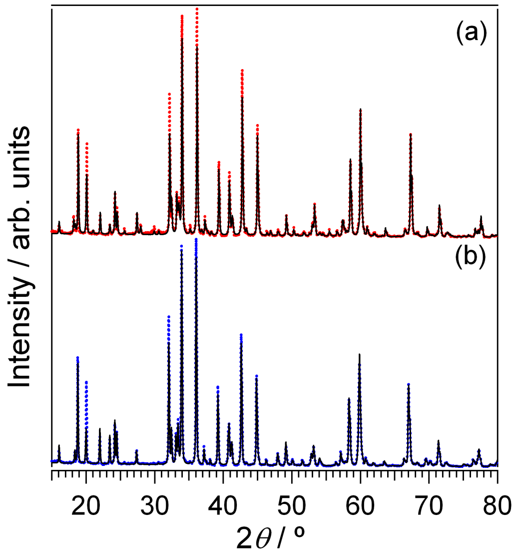

Figure 5.44: XRD patterns of LMA: 2%Mn^{2+}, 5%Yb^{3+} (a) and LMnA: 1%Yb^{3+} (b). Colored dots show the experimental data and black lines the Rietveld refinements.

LMA microcrystalline samples doped with nominal concentrations of 1%Mn^{2+}-1%Yb^{3+}, 2%Mn^{2+}-5%Yb^{3+}, and $LaMnAl_{11}O_{19}$ (LMnA) doped with 1%Yb^{3+} have been prepared by the precipitation method described in Section 3.6. LMA: 1%Mn^{2+}, 1%Yb^{3+} has also been synthesized by a combustion route. XRD patterns of 2%Mn^{2+}-5%Yb^{3+} co-doped LMA and 1%Yb^{3+}-doped LMnA are shown in Fig. 5.44. Both patterns indicate a fairly good crystallization of synthesized powders in the *magnetoplumbite* structure [54]. For the structural refinement, the "vacancy model" published by Iyi *et al.* on a lanthanum hexa-aluminate compound has been exploited [55].

The Rietveld refinement of the LMA: 2%Mn^{2+}, 5%Yb^{3+} XRD pattern is consistent with the *magnetoplumbite* structure with lattice parameters a=5.5602(5) Å and c=22.055(4) Å, but also reveals small traces (∼4% volume fraction) of Al_2O_3 ($R-3c$ space group). Similarly, the XRD pattern of LMA: 1%Mn^{2+}, 1%Yb^{3+} (data not shown) reveals the *magnetoplumbite* structure with lattice parameters a=5.5678(2) Å and c =22.026(2) Å of the as obtained powders, and traces of Al_2O_3 are also detected. The divalent ion occupies exclusively the 4f site (0.5 occupancy factor) together with an Al^{3+} ion and both ions are tetrahedrally coordinated by oxygens with a C_{3v} point symmetry [52].

For the LMnA powders containing Mn^{2+} instead of Mg^{2+} similar results are obtained;

97% of LMnA *magnetoplumbite* structure and small traces of Al_2O_3. Mn^{2+} ions also occupy only the 4f site (C_{3v} symmetry) [56]. For this phase the refined cell parameters are: $a = 5.5818(5)$ and c=22.070(3) Å. The increased cell parameters observed for LMnA in comparison with LMA reflect the bigger ionic radius of Mn^{2+} with respect to Mg^{2+}.

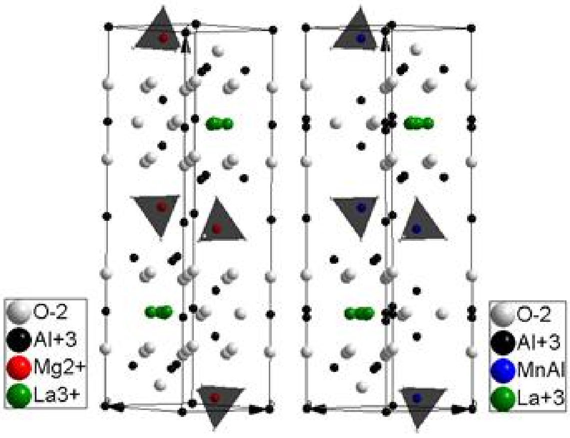

Figure 5.45: Unit cells for LMA (left) and LMnA (right) crystals. The tetrahedral coordination of Mg^{2+} or Mn^{2+} by oxygens is illustrated.

The unit cells of the LMA and LMnA crystal structures are shown in fig. 5.45. There are two different sites for the lanthanides in both LMA and LMnA phases. In the LMA sample, the principal site (0.49 occupancy) has D_{3h} symmetry and a 12-fold coordination number, whereas the satellite La site (0.115 occupancy) has a lower point symmetry (C_{2v}) [52]. In the case of LMnA compound, the satellite La site has the same point symmetry as in LMA, but with lower occupancy factor (0.05), whereas there is a change in the point symmetry (from D_{3h} to C_s) in the principal La site. From our structural refinement the following distances are obtained: La(1)-Mg=5.844 Å and La(2)-Mg=5.728 Å for LMA and La(1)-Mn=5.795 Å and La(2)-Mn=5.724 Å for LMnA. The shortest La-La distance is 11.337 Å and 11.324 Å for LMA and LMnA, respectively. All these distances are relevant for Mn^{2+}-Yb^{3+} interaction and the subsequent energy transfer process.

Optical properties

Luminescence, excitation and lifetime measurements have been carried out on different Mn^{2+}-Yb^{3+} co-doped LMA samples. An extended spectroscopic investigation to clarify the effects of Mn^{2+} and Yb^{3+} concentrations as well as temperature on UC luminescence properties is presented.

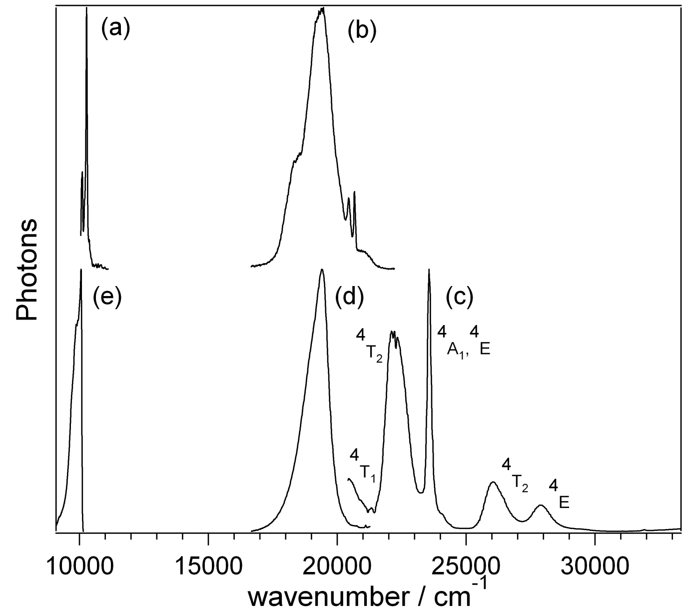

Figure 5.46: RT spectra of LMA: 1%Mn^{2+}, 1%Yb^{3+}. IR excitation Yb^{3+} spectrum detecting Mn^{2+} UC emission (a) $^4T_1 \rightarrow {}^6A_1$ Mn^{2+} UC luminescence after IR excitation at 10250 cm^{-1} (b). RT Mn^{2+} direct excitation spectrum monitoring the Mn^{2+} emission at 19455 cm^{-1} (c). Mn^{2+} peaks are labeled according to the Tanabe-Sugano diagram for tetrahedral Mn^{2+} with Δ=5840 cm^{-1} and B=730 cm^{-1}. Mn^{2+} emission spectrum after direct excitation at 424 nm (d). RT $^2F_{5/2} \rightarrow {}^2F_{7/2}$ Yb^{3+} luminescence (e).

- **Synthesis method and concentration dependence.**

Figure 5.46(b) and (d) shows the RT Mn^{2+} luminescence spectra of LMA microcrystals prepared by precipitation and doped with 1%Mn^{2+} and 1%Yb^{3+} upon IR and visible excitation, respectively. The green broad band emission extended from 17000 to 20500 cm^{-1}, is assigned to the $^4T_1 \rightarrow {}^6A_1$ Mn^{2+} transition in tetrahedral coordination, and the high energy peaks observed in the UC spectra (Fig. 5.46(b)), are due to Yb^{3+}-Yb^{3+} cooperative luminescence [57], [58], [59], [60]. As far as we know, this is the first observation of green Mn^{2+} UC luminescence upon Yb^{3+} excitation at RT. Figure 5.46(a) shows the excitation spectrum in the IR region of the Mn^{2+} UC luminescence detecting at 19455 cm^{-1}. Figure 5.46(c) shows the RT excitation spectrum of the $^4T_1 \rightarrow {}^6A_1$ Mn^{2+} luminescence which proves the assignment of the green luminescence to a Mn^{2+} ion in tetrahedral coordination. Figure

5.46(e) displays the $^2F_{5/2} \rightarrow {}^2F_{7/2}$ Yb^{3+} emission of the LMA: 1%Mn^{2+}, 1%Yb^{3+} upon excitation at 10250 cm^{-1}.

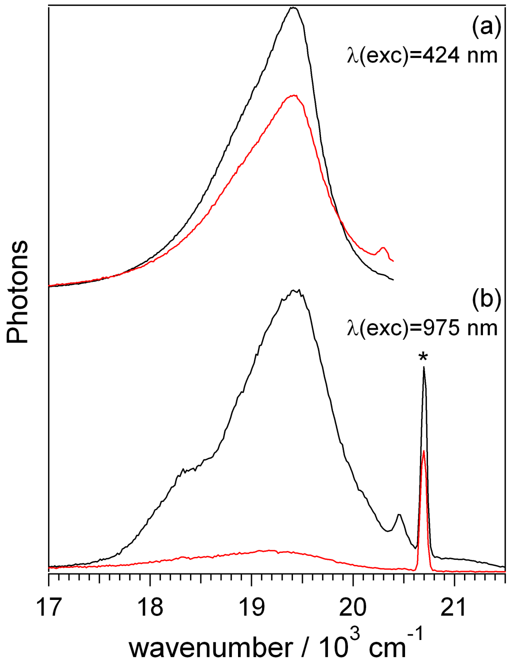

Figure 5.47: RT luminescence spectra of LMA: 1%Mn^{2+}, 1%Yb^{3+} prepared by precipitation (black) and combustion (red) upon excitation at 23580 cm^{-1} (a) and 10250 cm^{-1} (b). * is an artifact and represents the laser at twice the excitation frequency. Measurements were carried out under the same experimental conditions.

Since high purity green UC luminescence from tetrahedrally coordinated Mn^{2+} ions has been demonstrated in LMA: 1%Mn^{2+}, 1%Yb^{3+} upon Yb^{3+} excitation, we have performed different attempts to increase the UC efficiency by changing the synthesis method or the dopant concentration. Figure 5.47 compares the RT luminescence spectra of LMA: 1%Mn^{2+}, 1%Yb^{3+} micropowders prepared by precipitation and combustion upon visible and IR excitation. It can be observed that for both excitation energies the sample prepared by precipitation has higher luminescence intensity than the one by combustion. Moreover, UC emission intensity is about an order of magnitude higher for precipitation powders. Figure 5.48 compares the RT luminescence spectra of co-doped LMA prepared by precipitation for different Mn^{2+} and Yb^{3+} concentrations upon visible and IR excitation. No shift in energy or change in bandwidth is observed comparing the Mn^{2+} luminescence after direct and UC

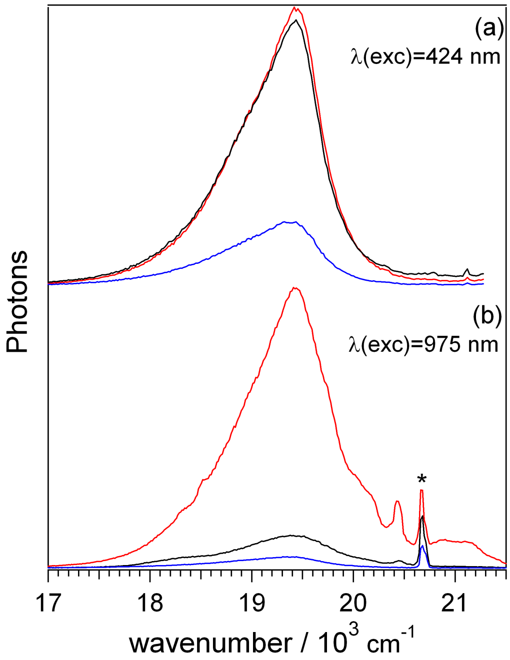

Figure 5.48: RT luminescence of Mn^{2+}-Yb^{3+} co-doped LMA upon excitation at 23580 cm^{-1} (a) and 10250 cm^{-1} (b) for the following concentrations: 1%Mn^{2+}-1%Yb^{3+}(black), 2%Mn^{2+}-5%Yb^{3+} (red) and 99%Mn^{2+}-1%Yb^{3+} (blue). * is a laser artefact appearing at twice the excitation frequency. Measurements were carried out under the same experimental conditions.

excitation. Considering the Mn^{2+} sensitivity to surrounding, this indicates that both direct and UC luminescence are originated from Mn^{2+} ions having the same environment, what is an indication of the homogenous distribution of Mn^{2+} and Yb^{3+} impurities in LMA. The green Mn^{2+} emission in LMA: 2%Mn^{2+}, 5%Yb^{2+} is centered at 19430 cm^{-1} while the same band appears about 50 cm^{-1} towards higher energy for LMnA: 1%Yb^{3+} according to expectations due to the smaller ionic radius of Mg^{2+} compared to Mn^{2+}.

It is worth noting that Mn^{2+} emission is obtained for all doping concentrations upon excitation in both 23580 cm^{-1} and 10250 cm^{-1} bands even above RT. For direct Mn^{2+} excitation (Fig. 5.48(a)), the RT luminescence intensity ratio of the pure manganese compound (LMnA) to the Mn^{2+}-doped LMA has been found to be approximately 1:5, while the intensity for 1%Mn^{2+} and 2%Mn^{2+} compounds is roughly the same. This drastic reduction of emission intensity could be initially ascribed to thermally activated energy migration and partial trapping into non-luminescent impurities as commonly occurs in concentrated manganese systems. Figure 5.48(b) shows that UC intensity in 2%Mn^{2+}-5%Yb^{3+} co-doped LMA is about an order of magnitude higher than the UC in 1%Mn^{2+}-1%Yb^{3+} co-doped LMA. Considering crystalline quality and emission efficiency, LMA co-doped with 2%Mn^{2+} and 5%Yb^{3+} doping level and prepared by precipitation provides an optimum efficient UC system.

- **Temporal evolution.**

The temporal evolution of the RT $^4T_1 \rightarrow {}^6A_1$ Mn^{2+} green luminescence has been recorded after direct Mn^{2+} excitation into the $^4A_1$, ^4E levels at 23580 cm^{-1}, and IR excitation into the $^2F_{7/2} \rightarrow {}^2F_{5/2}$ Yb^{3+} transition at 10205 cm^{-1}, with 10 ns short pulses for LMA: 1%Mn^{2+}, 1%Yb^{3+}, LMA: 2%Mn^{2+}, 5%Yb^{3+} and LMnA: 1%Yb^{3+} samples (Fig. 5.49). The intensity time-dependence of the Mn^{2+} emission after visible excitation shows a single exponential decay with lifetimes of τ=6.2 ± 0.1 ms for LMA: 1%Mn^{2+}, 1%Yb^{3+} and LMA: 2%Mn^{2+}, 5%Yb^{3+}, and τ=3.8 ± 0.1 ms for LMnA: 1%Yb^{3+} (Fig. 5.49(a), (b) and (c)). However, the time dependence of the UC Mn^{2+} luminescence after IR excitation presents a different behavior comparing diluted and undiluted systems. A single exponential decay is observed in LMA: 1%Mn^{2+}, 1%Yb^{3+} (τ=5.8 ± 0.2 ms, Fig. 5.49(d)) and LMA: 2%Mn^{2+}, 5%Yb^{3+} (τ=5.2 ± 0.2 ms, Fig. 5.49(e)). This lifetime is significantly faster than the one obtained by direct Mn^{2+} excitation (τ=6.2 ms) as it was previously observed in Yb^{3+}-doped $RbMnCl_3$. It is probably related to an increase in the emission probability due to the Mn^{2+}-Yb^{3+} interaction, or to an additional $Mn^{2+} \rightarrow Yb^{3+}$ decay path, within the UC-efficient clusters [49]. In the case of LMnA: 1%Yb^{3+}, a luminescence intensity rise before decaying is clearly detected (Fig 5.49(f)). These differences are crucial to identify the UC mechanism involved in these systems as it will be discussed later on.

Figure 5.50 shows the temporal evolution of the Yb^{3+}-Yb^{3+} cooperative luminescence in LMA: 2%Mn^{2+}, 5%Yb^{3+} upon IR modulated excitation at 10205 cm^{-1} at 15 K (a) and RT (b). The decay can be described by a single exponential function

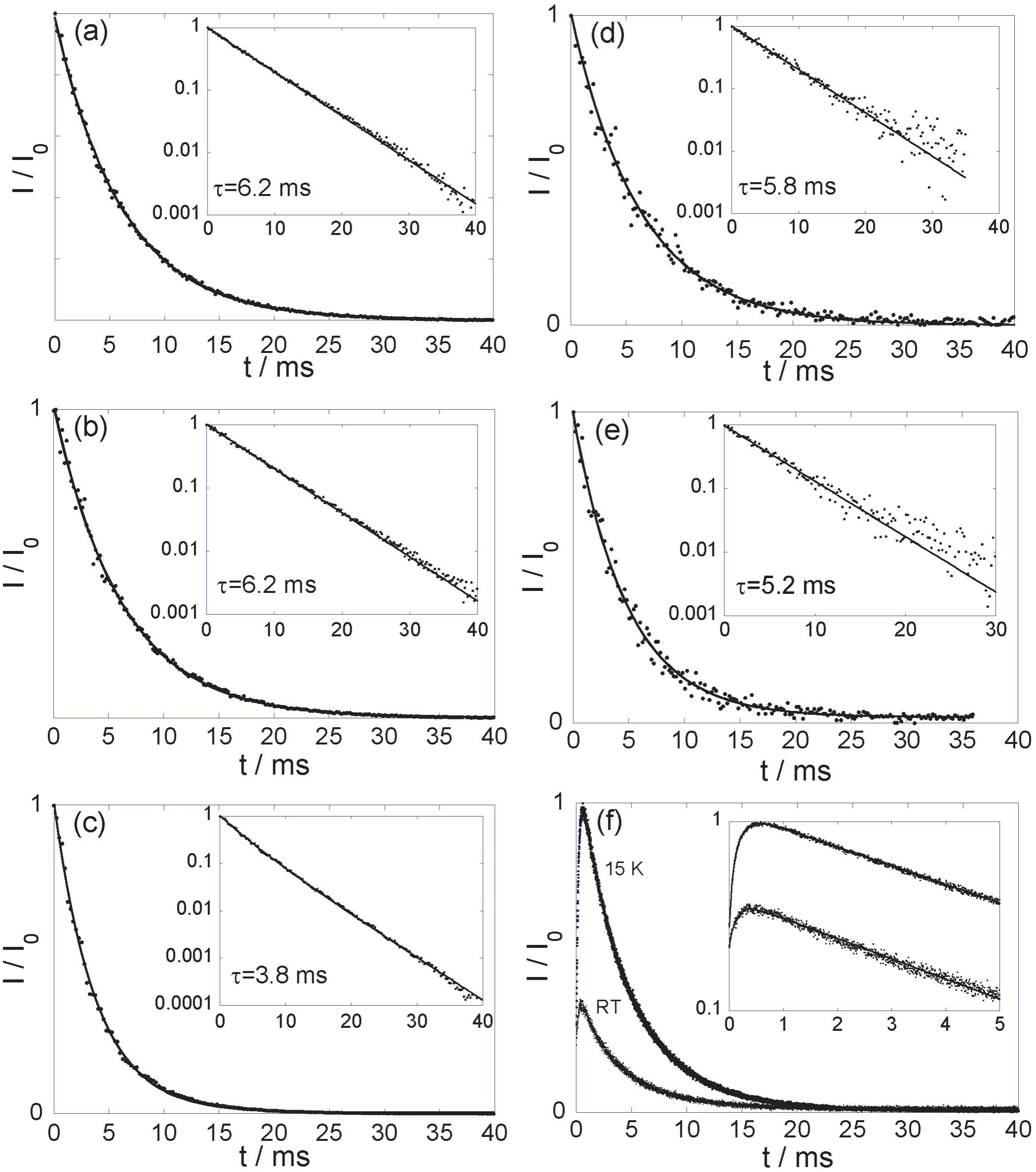

Figure 5.49: RT temporal evolution of the normalized Mn^{2+} ${}^4T_1 \rightarrow {}^6A_1$ emission intensity after pulsed excitation at 23580 cm^{-1} in LMA: 1%Mn^{2+}, 1%Yb^{3+} (a), LMA: 2%Mn^{2+}, 5%Yb^{3+} (b) and LMnA: 1%Yb^{3+} (c). And temporal behavior of the Mn^{2+} UC emission after pulsed excitation at 10205 cm^{-1} in LMA: 1%Mn^{2+}, 1%Yb^{3+} (d), LMA: 2%Mn^{2+}, 5%Yb^{3+} (e) at RT, and LMnA: 1%Yb^{3+} (f) at both 15 K and RT. The insets show the same data in semi-logarithmic scale. Continuous lines are the results of different fitting procedures (see text).

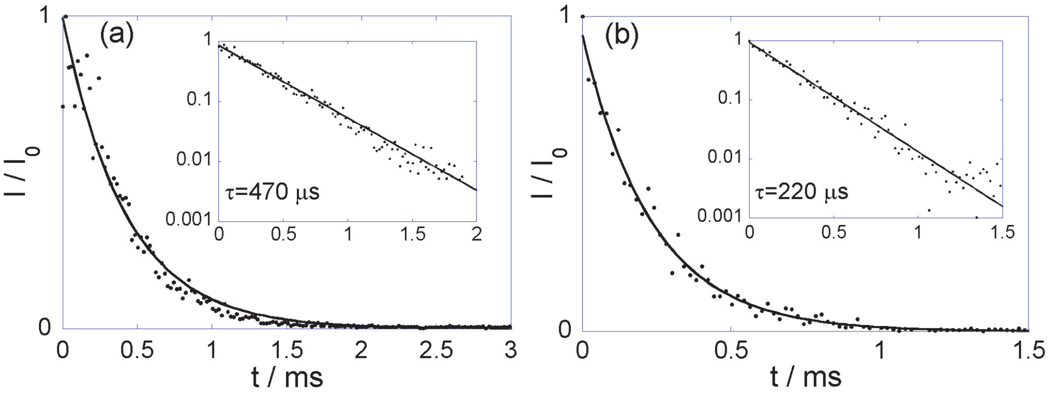

Figure 5.50: Temporal behavior of the normalized Yb^{3+}-pairs emission in LMA: 2%Mn^{2+}, 5%Yb^{3+} after pulsed excitation at 10205 cm^{-1} at 15 K (a) and RT (b). The insets show the same data in semi-logarithmic scale.

with lifetimes of τ=470 ± 10 μs at 15 K and τ=220 ± 10 μs at RT.

In LMA: 2%Mn^{2+}, 5%Yb^{3+} a lifetime of 5.2 ms has been obtained for the Mn^{2+} UC emission (Fig. 5.49(e)) while the RT lifetime of Yb^{3+}-Yb^{3+} cooperative luminescence is 220 μs (Fig. 5.50(b)). Since both lifetimes differ by an order of magnitude, we can separate both UC luminescence by time-resolved spectroscopy. Figure 5.51 shows both Mn^{2+} green emission (broad band centered at 19430 cm^{-1}) and Yb^{3+}-pairs luminescence (higher energy peaks above 19500 cm^{-1}) upon IR excitation at 10205 cm^{-1} taken at different delay times after the excitation pulse. It can be seen that the Yb^{3+}-Yb^{3+} cooperative emission intensity decreases much faster than the Mn^{2+} UC luminescence intensity according to their lifetimes. The figure clearly illustrates this phenomenon showing the rapid decay of Yb^{3+}-pairs luminescence in a ms time scale while the Mn^{2+} UC emission remains almost constant for this time.

- **Temperature dependence.**

The temperature dependence of luminescence intensity and lifetime presents different trends for co-doped LMA at low concentrations of Mn^{2+} and pure LMnA microcrystalline samples. Figure 5.52 shows the temperature dependence of the normalized emission intensity (I/I_{max}) and the lifetime (τ) of the ${}^4T_1 \rightarrow {}^6A_1$ Mn^{2+} transition in LMA: 2%Mn^{2+}, 5%Yb^{3+} and LMnA: 1%Yb^{3+} upon IR excitation at 10205 cm^{-1} in the 15-600 K range. It must be noted that for LMA: 2%Mn^{2+},

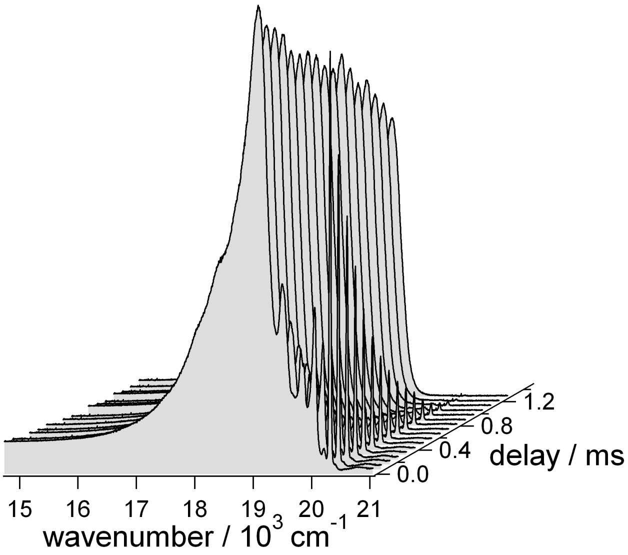

Figure 5.51: 15 K UC time-resolved emission of LMA: 2%Mn^{2+}, 5%Yb^{3+} exciting at 10205 cm^{-1} using different delay times after the short excitation pulse.

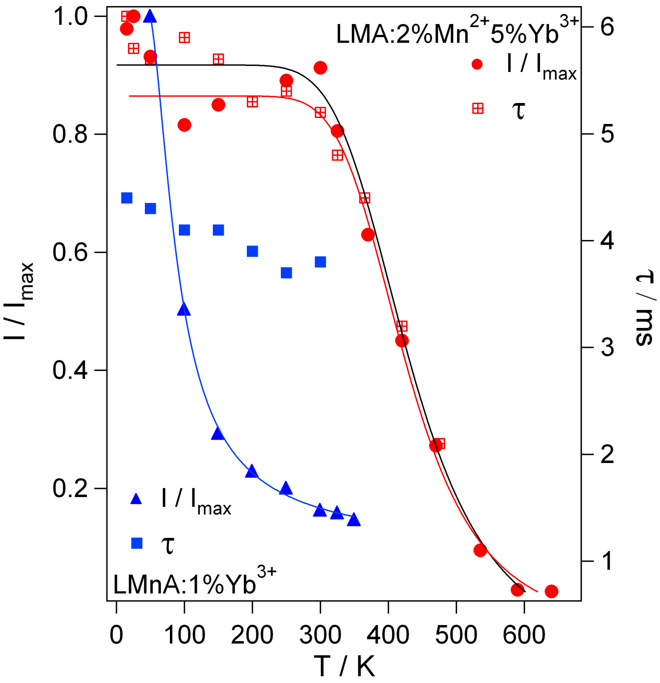

Figure 5.52: Temperature dependence of the normalized Mn^{2+} UC luminescence intensity (red circles) and Mn^{2+} UC emission lifetime (open red squares) in LMA: 2%Mn^{2+}, 5%Yb^{3+}. And temperature dependence of the normalized Mn^{2+} UC luminescence intensity (blue triangles) and Mn^{2+} UC emission lifetime (blue squares) in LMnA: 1%Yb^{3+} after 10205 cm^{-1} excitation. The lines correspond to fittings according to eqs. 5.2, 5.3 and 5.4 (see text).

5%Yb^{3+} the UC luminescence intensity remains almost constant up to RT. Although above this temperature the quenching process becomes important and the UC luminescence intensity starts to decrease, it still remains up to 600 K. The associated UC lifetime follows a similar trend; it diminishes slightly from 10 to 300 K and steeply decreases above this temperature. Both the intensity and the lifetime have a similar behavior pointing out the non-radiative character of the UC luminescence decrease. An analogous behavior is detected for both lifetime and intensity in LMA: 1%Mn^{2+}, 1%Yb^{3+} (data not shown for clarity). The quenching process of the Mn^{2+} UC luminescence is rather different in LMnA: 1%Yb^{3+} as shown in Fig. 5.52. As it usually happens in concentrated materials, the Mn^{2+} emission is thermally quenched at much lower temperatures (T <100 K) than in Mn^{2+} diluted samples. This is an intrinsic behavior of concentrated manganese and it is usually accompanied by a similar lifetime decrease with temperature [51], [61]. However, since in this case the lifetime remains pretty constant until RT, the reduction in the intensity due to migration and subsequent quenching is unlikely. Instead, the photoluminescence dwindle above 100 K which is induced either by direct excitation into the $^4A_1$, ^4E Mn^{2+} state or via UC in LMnA: 1%Yb^{3+}, must be ascribed to a decrease in the effective Mn^{2+} excitation with temperature. As it is shown below, this puzzling $I(T)$ behavior between 0 and 300 K can be phenomenologically described through a thermal deactivation process for Mn^{2+} excitation.

In order to model Mn^{2+} luminescence in LMA: 2%Mn^{2+}, 5%Yb^{3+} let us assume that the radiative lifetime, τ_R, does not change significantly with temperature. According to a model proposed by Mott, thermally activated non-radiative processes can be described by an activation energy, E_a, with a pre-exponential frequency factor, p [62]. Consequently, the lifetime and intensity dependence on temperature have been fitted according to Eqs. 5.2 and 5.3. In both cases the fitted parameters are E_a = 0.26 eV and p = 180×10^3 s^{-1} for LMA: 2%Mn^{2+}, 5%Yb^{3+}.

$$\tau(T) = \frac{1}{\frac{1}{\tau_R} + p \cdot \exp(-E_a/K_B T)} \tag{5.2}$$

$$\frac{I(T)}{I_{max}} = \frac{1}{1 + p \cdot \tau_R \exp(-E_a/K_B T)} \tag{5.3}$$

It must be mentioned that this simple model explains why $I(T)$ and $\tau(T)$ behave with temperature in the same manner. Both the activation energy ($E_a = 0.26$ eV) and the Mn^{2+} dilution suggest that the non-radiative process is associated with multiphonon relaxation within (MnO_4) units. In this analysis, it is assumed that the excited Mn^{2+} via either UC or direct excitation is approximately temperature independent. Nevertheless, in the case of LMnA: 1%Yb^{3+}, eq. 5.3 must account for the fraction of excited Mn^{2+} as a function of temperature: $E_R(T) = [\mathrm{Mn}](T)/[\mathrm{Mn}](0)$ with [Mn] being the concentration of excited Mn^{2+}. Hence, eq. 5.3 transforms to

$$\frac{I(T)}{I_{max}} = \frac{E_R(T)}{1 + p \cdot \tau_R \exp(-E_a/K_B T)} \tag{5.4}$$

On the assumption that the up-converted Mn^{2+} does not change with temperature ($E_R = 1$), we then obtain the same variation for $I(T)$ and $\tau(T)$ as eq. 5.2 and 5.3. However, this is not the case if E_R varies with temperature. The $I(T)$ reduction above 100 K observed in LMnA: 1%Yb^{3+} keeping $\tau(T)$ constant up to RT, can be explained through this model if we consider that Mn^{2+} excitation is thermally deactivated: $E_R = (1 - \alpha \exp(-\Delta/K_B T))$ where Δ is the activation energy and α is the pre-exponential factor. The experimental $I(T)$ data (blue) behaves in this way for values of $\Delta = 5.6$ meV and $\alpha = 1.2$. Although the present model makes the reduction of intensity and the lifetime constancy compatible, its microscopic origin is unclear. This thermal behavior is unusual for Mn^{2+} concentrated systems in which $I(T)$ correlates with $\tau(T)$.

- **UC mechanism.**

The RT ${}^4T_1 \rightarrow {}^6A_1$ Mn^{2+} UC luminescence intensity versus the excitation power density at 10250 cm^{-1} for LMA: 2%Mn^{2+}, 5%Yb^{3+} is plotted on a double logarithmic scale in Fig. 5.53. This system presents a quadratic power dependence below 1.5 Wcm^{-2} which is the typical behavior of a two-photon excitation process in the

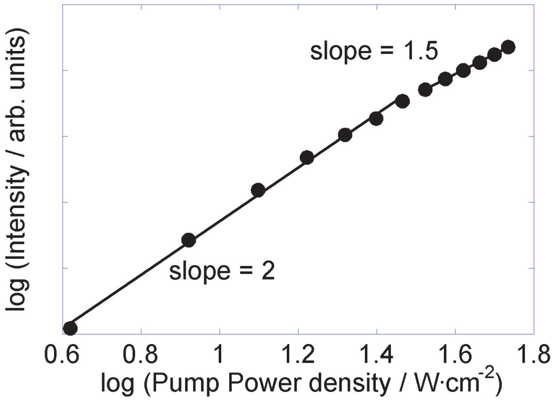

Figure 5.53: Excitation power density dependence of the RT Mn^{2+} UC emission in LMA: 2%Mn^{2+}, 5%Yb^{3+} upon excitation with a LD at 10250 cm^{-1}.

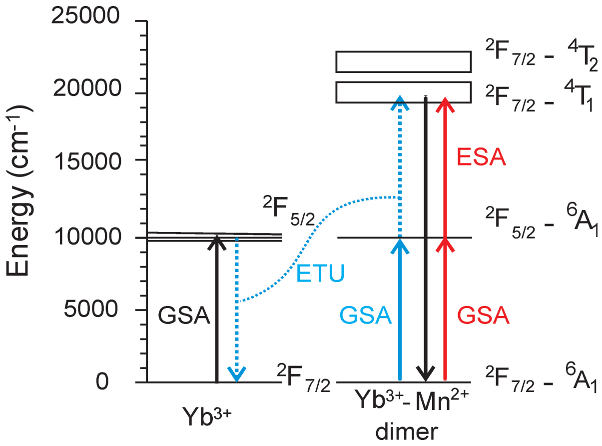

Figure 5.54: Energy level diagram in a Mn^{2+}-Yb^{3+} dimer notation with the Mn^{2+} emission and the proposed UC mechanisms.

low-power regime. The slope decreases from 2 to 1.5 at higher excitation power densities as explained before [24], [25]. Since excitation occurs into $^2F_{5/2}$ Yb^{3+} states, and emission takes place from $^4T_1$ Mn^{2+} states, the active UC mechanism in the three studied samples, LMA: 1%Mn^{2+}, 1%Yb^{3+}, LMA: 2%Mn^{2+}, 5%Yb^{3+} and LMnA: 1%Yb^{3+} must involve the participation of both Yb^{3+} and Mn^{2+} ions. Mn^{2+} has no intermediate resonant states with Yb^{3+}; hence, GSA/ESA and GSA/ETU mechanisms in pure ions must be ruled out in these systems. A simple model based on an exchange-coupled Mn^{2+}-Yb^{3+} dimer state was previously proposed to explain the experimental behavior in Yb^{3+}-doped $RbMnCl_3$, $CsMnBr_3$ and $CsMnCl_3$ [47], [49].

The UC emission in LMA: 1%Mn^{2+}, 1%Yb^{3+} and LMA: 2%Mn^{2+}, 5%Yb^{3+} (Fig. 5.49 (d) and (e)) shows an immediate decay after the laser pulse with no rise due to energy transfer longer than 80 ns (low detection limit). According to the LMA crystal structure (Fig. 5.45), the shortest Mn^{2+}-Yb^{3+} distance for Mn^{2+}-O-O'-Yb^{3+} dimers in Mn^{2+}-Yb^{3+} co-doped LMA is 5.728 Å. In agreement with Luzón *et al.* and Hehlen and co-workers, superexchange distances can be as long as 6-8 Å; thus, dimers in co-doped LMA are able to exhibit a superexchange pathway [63], [64]. Taking into consideration a GSA/ESA-type mechanism in Mn^{2+}-Yb^{3+} dimers, the GSA step is predominantly a single ion process in Yb^{3+}, but the ESA step requires the mixing of Mn^{2+} and Yb^{3+} states. The rise of the emission intensity after the excitation pulse in LMnA: 1%Yb^{3+} (Fig. 5.49(f)) evidences the contribution of some non-radiative energy transfer process after the pulse to the UC mechanism. The involved processes can be GSA/ETU in a dimer or cooperative sensitization. Once more, the Mn^{2+}-Yb^{3+} distance in LMnA (5.724 Å) is short enough to allow dimer formation, hence we propose the GSA/ETU as the actual mechanism. The Mn^{2+} lifetime is shorter in LMnA: 1%Yb^{3+} than in 1% or 2% Mn^{2+}-doped LMA; this evidences a larger exchange contribution for the pure manganese system. The fact that the intensity rise does not start from zero is noteworthy. This implies that there must be an additional excitation within the duration of the laser pulse governed by a GSA/ESA mechanism and it is another evidence of dimer formation. Considering that the lifetime of the $^2F_{7/2} - {}^4T_1$ dimer state (see Fig. 5.54) is approximately the same as Mn^{2+} lifetime after direct excitation, it is possible to estimate the GSA/ESA and GSA/ETU contributions to the total intensity as we have done for Y_2O_3: Er^{3+}, Yb^{3+} nanoparticles (Section 5.2.1) [19]. At 15 K, about 23% of the total UC luminescence is due to excitation within the pulse, GSA/ESA, while contributions of 33% and 67% have been obtained at RT for GSA/ESA and GSA/ETU mechanisms respectively.

Figure 5.54 shows a schematic representation of an exchange-coupled Mn^{2+}-Yb^{3+} dimer and an Yb^{3+} nearby monomer along with the proposed mechanisms for the UC luminescence; GSA/ESA for LMA: 1%Mn^{2+}, 1%Yb^{3+} and LMA: 2%Mn^{2+}, 5%Yb^{3+}

and both GSA/ESA and GSA/ETU for LMnA: 1%Yb^{3+}. The dimer intermediate state are dominantly localized on Yb^{3+} while the higher excited states are mainly localized on Mn^{2+} ions [49].

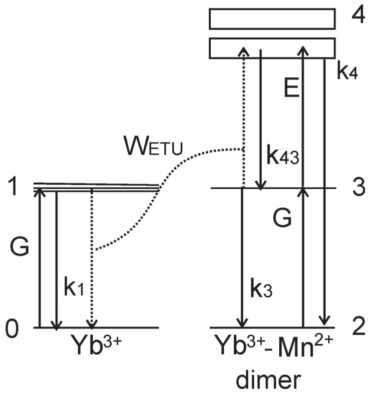

Figure 5.55: Relevant levels involved in the GSA/ESA and GSA/ETU UC processes in LMnA: 1%Yb^{3+}.

The temporal evolution of the LMnA: 1%Yb^{3+} can be simulated considering GSA/ESA and GSA/ETU mechanisms according to the five level system shown in Fig. 5.55 involving an Yb^{3+} ion and a Mn^{2+}-Yb^{3+} dimer. Within this model, the coupled differential rate equations describing the population of each level, N_i can be written as:

$$\begin{aligned}
\frac{dN_0}{dt} &= -GN_0 + \frac{N_1}{\tau_1} + W_{\mathrm{ETU}}N_1N_3 \\
\frac{dN_1}{dt} &= GN_0 - \frac{N_1}{\tau_1} - W_{\mathrm{ETU}}N_1N_3 \\
\frac{dN_2}{dt} &= -GN_2 + \frac{N_3}{\tau_3} + \frac{N_4}{\tau_4} \\
\frac{dN_3}{dt} &= GN_2 - \frac{N_3}{\tau_3} - EN_3 + \frac{N_4}{\tau_{43}} - W_{\mathrm{ETU}}N_1N_3 \\
\frac{dN_4}{dt} &= EN_3 - \frac{N_4}{\tau_{43}} + W_{\mathrm{ETU}}N_1N_3 - \frac{N_4}{\tau_4}
\end{aligned} \tag{5.5}$$

where τ_i represents the lifetime of each level N_i, G and E are the power dependent GSA and ESA rate constants, respectively, and W_{ETU} is the two-center energy-transfer process parameter. τ_1 and τ_3 are known from the experimentally measured Yb^{3+} lifetime; 940 μs at 15 K and 370 μs at RT, which are significantly longer than those obtained for LMA: 2%Mn^{2+}, 5%Yb^{3+}, while τ_4 is the Mn^{2+} emission lifetime; 4.4 ms at 15 K and 3.8 ms at RT. By fitting the time dependent evolution of the UC luminescence in LMnA: 1%Yb^{3+} to this set of equations, we obtain an energy transfer rate, $W_{\mathrm{ETU}}N_1N_3$, of 2310 s^{-1} and 3125 s^{-1} for RT and 15 K respectively (Fig. 5.49(f)).

Nevertheless, the UC intensity evolution depicted in Fig. 5.49(f) can be expressed in terms of Mn^{2+} and Yb^{3+} lifetimes. In fact, the rate equation for $N_4(t \geq 0)$ can be solved analytically under the assumption that Yb^{3+} populations, N_1 and N_3, are similar ($N_1 \approx N_3$), both decaying as $N_3 = N_3^0 \exp(-t/\tau_3)$. This approximation yields the following time-dependent Mn^{2+} population: $N_4 = N_4^0(\exp(-t/\tau) - \alpha \exp(-2t/\tau_3))$. The parameter $\frac{1}{\tau} = \frac{1}{\tau_4} + \frac{1}{\tau_{43}}$, governing the temporal decay of Fig. 5.49(f), is directly related to the Mn^{2+} lifetime, whereas τ_3 controls the intensity rise after $t = 0$. The parameters α and N_4^0 determines the Mn^{2+} population at $t = 0$ due to GSA/ESA. By fitting the intensity temporal dependence in Fig. 5.49(f) to this approximate equation, the following parameters are obtained: $\tau = 4.2$ ms and $\tau_3 = 960$ μs at RT, and $\tau = 4.7$ ms and $\tau_3 = 435$ μs at 15 K. These values are quite similar to Mn^{2+} and Yb^{3+} lifetimes, respectively, what supports the proposed UC GSA/ETU mechanism in LMnA: 1%Yb^{3+}.

Conclusions

The spectroscopic study carried out on LMA microcrystals doped with different Mn^{2+} and Yb^{3+} concentrations indicates that Mn^{2+} UC luminescence is very efficient in these systems even at RT. LMA crystallizes with the *magnetoplumbite* crystal structure where Mn^{2+} ions are tetrahedrally coordinated by oxygen atoms. Mn^{2+} UC luminescence and Yb^{3+}-pairs emission have been detected in all samples. It has been demonstrated that UC luminescence takes place via GSA/ESA mechanism for LMA: 1%Mn^{2+}, 1%Yb^{3+} and LMA: 2%Mn^{2+}, 5%Yb^{3+}, whereas an additional GSA/ETU contribution participates in LMnA: 1%Yb^{3+}. This conclusion is based on time-resolved spectroscopy and impurity concentration dependent experiments. The theoretical rate equations model confirm the different proposed UC mechanisms involving Mn^{2+}-Yb^{3+} dimer formation. In all LMA and LMnA systems the luminescence via UC is observed up to RT and above 500 K in the case of LMA: 2%Mn^{2+}, 5%Yb^{3+}, being this UC emission an order of magnitude stronger than any other. Mn^{2+} UC luminescence in LMA: 2%Mn^{2+}, 5%Yb^{3+} remains very intense up to RT but at higher temperatures both the emission intensity and lifetime decrease in a similar manner, pointing out the non-radiative character of the quenching. On the contrary, an unusual decrease in the Mn^{2+} luminescence above 100 K with a constant lifetime has been detected in LMnA: 1%Yb^{3+}. This cannot be ascribed to Mn^{2+} migration and subsequent quenching, and it must be related to a decrease of Mn^{2+} pumping efficiency.

5.4 Transition-metal ions doped nanoparticles

Optical properties of materials containing TM ions depend on different factors such as site symmetry and crystal-field strength. The application of high pressure to these systems changes the crystal-field strength experienced by the TM ion, and it may also modify the symmetry. Hence, it is a powerful tool to obtain information about TM luminescent properties by continuously changing bond distances as well as crystal-field strengths or covalency [65].

Depending on the crystal-field strength, the lowest Cr^{3+} emitting level can be the $^4T_2$ or the ^2E state (see Fig. 2.5) [51]. Each excited state exhibits different luminescence properties due to the different electron-lattice coupling. Typical emission features for the weak crystal-field case are a fast decay and broad emission band due to the spin-allowed $^4T_2 \rightarrow {}^4A_2$ transition. In contrast, the narrow R-lines emission associated with the spin-forbidden transition from the ^2E level to the $^4A_2$ ground state is expected for the strong crystal-field scenario. An interesting situation arises for intermediate crystal-field, when the crystal-field strength on Cr^{3+} ions is near the $^4T_2 - {}^2E$ excited-state crossover (ESCO), and the energy separation between both states is small. In this case, the $^4T_2$ state may interact with the ^2E state through thermal population effects [66] or through spin-orbit coupling [67], and the lowest emitting state is a mixture of both excited levels [65]. The effect of the $^2T_1$ state has been neglected in this work for simplicity. Oxide garnets are attractive host materials to investigate ESCO processes since they provide intermediate crystal-fields around Cr^{3+} which are close to the $^4T_2$-^2E crossing point, resulting in a strong coupling of the excited states [68]. Concretely, in bulk GGG: Cr^{3+}, the $^4T_2$ state has been seen to be located approximately 300-400 cm^{-1} above the ^2E level (see Fig. 2.5) [69], [70].

The luminescence spectra associated with the $^2E \rightarrow {}^4A_2$ transition of octahedral Cr^{3+} in YAG: Cr^{3+} single crystal was investigated by Wall *et al.* as a function of temperature [66]. The spectra presented sharp R-lines $^2E \rightarrow {}^4A_2$ emission, as well as low energy sidebands. These sidebands were more important at higher temperatures and their nature was discussed since it could be attributed to both vibronic transitions and exchange coupled Cr^{3+} pairs. These authors also pointed out another possibility; the emission from the $^4T_2$ state. However, only vibronic processes were established to be responsible for the sidebands in this case.

As it was mentioned before, the application of high pressure allows to continuously tune the Cr^{3+} crystal-field strength, and hence to investigate the $^2E - {}^4T_2$ coupling. Cr^{3+} ESCO was first observed by Dolan *et al.* in K_2NaGaF_6: Cr^{3+} at 6.1 GPa and 154 K [71]. Moreover, a complete change from broadband to ruby-like emission was observed in $LiCaAlF_6$: Cr^{3+} at RT and 28 GPa [67]. The RT high pressure luminescence study in bulk GGG: Cr^{3+} was carried out by Hömmerich *et al.* [69]. The emission spectra showed a broad band at ambient pressure, indicative of the $^4T_2 \rightarrow {}^4A_2$ transition, and the reduction of this broad band intensity accompanied by the increase of R-lines emission, $^2E \rightarrow {}^4A_2$, induced by the application of pressure up to 10 GPa. This change from broad band emission to ruby-like emission was correlated with the increase in the emission lifetime with pressure, corresponding to the transformation from the spin-allowed $^4T_2 \rightarrow {}^4A_2$ to the spin-forbidden $^2E \rightarrow {}^4A_2$ transition. As far as we know, no studies on GGG: Cr^{3+} nanoparticles under high pressure have been carried out so far.

5.4.1 Cr^{3+}-doped $Gd_3Ga_5O_{12}$

Synthesis and characterization

0.5%Cr^{3+}-doped GGG nanocrystals have been prepared by Pechini's method as described in Section 3.4. It was stated that for Nd^{3+}-Cr^{3+} co-doped GGG single crystals, Nd^{3+}

replaces Gd^{3+} sites while TM^{3+}, in particular Cr^{3+}, occupies Ga^{3+} sites [30]. Hence, unlike RE^{3+} doped GGG, the amount of Cr^{3+} ions (0.5% mol) is with respect to Ga^{3+}. From XRD patterns, the nanoparticles has been seen to exhibit the *garnet* structure with an average size of 30 nm, similarly to the case of lanthanides doped GGG (see Fig. 5.27).

Optical properties

Since Heer *et al.* detected UC emission at low temperatures in Cr^{3+}-Yb^{3+} co-doped $Y_3Ga_5O_{12}$ and YAG single crystals [48], [72], we initially focused on the UC luminescence study in GGG: Cr^{3+}, Yb^{3+} nanoparticles. However, no UC emission was detected in these samples even at low temperatures. Owing to the fact that the crystal-field strength on the Cr^{3+} site is very close to the ESCO, we have investigated in this work the optical properties of Cr^{3+}-doped GGG nanoparticles as a function of temperature and pressure in order to establish the effect of the ESCO on the optical behavior of nanocrystalline GGG. Luminescence and lifetime measurements have been performed on GGG: 0.5%Cr^{3+} nanoparticles in the 25-300 K range as well as under hydrostatic pressure up to 20 GPa at RT.

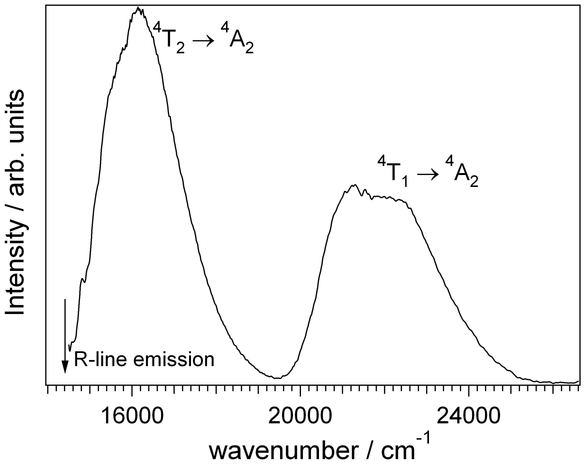

Figure 5.56: RT excitation spectrum of GGG: 0.5%Cr^{3+} detecting Cr^{3+} emission at 14085 cm^{-1}. The arrow corresponds to the R-lines emission energy.

The RT excitation spectrum of GGG: 0.5%Cr^{3+} nanoparticles monitoring luminescence at 14085 cm^{-1} is shown in Fig. 5.56. The two broad bands centered around

15800 and 21700 cm^{-1} correspond to the spin allowed $^4A_2 \rightarrow {}^4T_2$ and $^4A_2 \rightarrow {}^4T_1$ transitions respectively, in an octahedral environment, with $\Delta = 15800$ cm^{-1}, $B = 705$ cm^{-1} and $C = 2880$ cm^{-1}. The $\frac{\Delta}{B} = 22.4$ value is slightly higher than the ESCO ratio, $\frac{\Delta}{B}$(ESCO) $= 22$ (Fig. 2.5), close to the situation observed in the bulk.

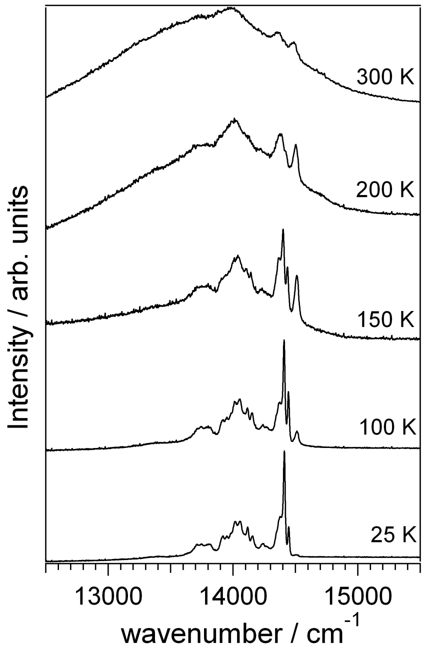

Figure 5.57: Temperature dependence of the GGG: 0.5%Cr^{3+} normalized luminescence spectra upon excitation at 21980 cm^{-1} at AP.

- **Temperature dependence.**

Figure 5.57 shows the temperature dependence of the luminescence spectra of GGG: 0.5%Cr^{3+} nanoparticles upon excitation at 21980 cm^{-1} in the 25-300 K range. At RT, only luminescence from the $^4T_2$ state is detected in other Cr^{3+}-doped garnets such as $Gd_3Sc_2Ga_3O_{12}$ or $La_3Lu_2Ga_3O_{12}$ [69], [73], or fluorides [67], according to the weaker crystal-field strength. In GGG on the contrary, since the $^4T_2$ state is situated above the ^2E one, besides the broadband emission due to the $^4T_2 \rightarrow {}^4A_2$ Cr^{3+} transition, sharp lines corresponding to the $^2E \rightarrow {}^4A_2$ emission are also observed. However, when temperature decreases, the intensity of the broad luminescence from $^4T_2$ is reduced, and its diminution is accompanied by the evolution of structured narrow R-lines emission. The pure $^4T_2$ emission almost disappears at 100 K and the

Table 5.8: Lifetimes of the GGG: 0.5%Cr^{3+} nanocrystals corresponding to the R-line and sidebands emission in the 25-300 K temperature range. The data for the bulk are extracted from Di Bartolo's presentation at the Spectroscopy Workshop (Erice 2010) [74].

T/K	τ/ms R-line (14410 cm^{-1})	τ/ms R-line bulk	τ/ms sidebands (13985 cm^{-1})	τ/ms sidebands bulk
25	1.68 ± 0.03	1.35	1.69 ± 0.04	1.20
50	1.65 ± 0.04	1.30	1.54 ± 0.03	1.15
100	1.21 ± 0.02	0.85	1.13 ± 0.04	0.80
150	0.59 ± 0.02	0.40	0.57 ± 0.02	0.40
200	0.34 ± 0.02	0.27	0.33 ± 0.03	0.27
250	0.27 ± 0.02	0.19	0.21 ± 0.03	0.19
300	0.19 ± 0.01	0.14	0.19 ± 0.03	0.14

spectra below that temperature show sharp R-line emission with the associated low energy bands. As it was discussed by Wall *et al.*, the sidebands in the Cr^{3+} spectra could be attributed to vibronic transitions, exchange coupled Cr^{3+} pairs, or emission from the $^4T_2$ state [66]. Cr^{3+} pairs emission can be ruled out in our case because of the low Cr^{3+} concentration, and the fact that some peaks appears up to 750 cm^{-1}. Surprisingly, the thermal behavior of Cr^{3+} luminescence is completely analogous to the Cr^{3+} emission spectra upon increasing pressure observed by Hömmerich *et al.* for bulk Cr^{3+}-doped GGG. In that work, the $^4T_2$ emission transformed into ^2E emission above 10 GPa (Fig. 2 in Ref. [69]).

The temporal evolution of the ruby-like Cr^{3+} luminescence (14410 cm^{-1}) as well as the emission from the sidebands (13985 cm^{-1}), after pulsed excitation with the OPO at 21980 cm^{-1} has been recorded in the 25-300 K temperature range. Experimental data have been fitted to a single exponential, $I(t) = I_0 \exp(\frac{-t}{\tau})$ and the best fits are shown in Table 5.8. The experimental lifetimes for nanocrystals have been compared with those reported for GGG: Cr^{3+} in bulk. The values in the case of the nanocrystals are significantly longer than those of the bulk (unknown concentration) [74].

It is important to point out that very similar values have been measured for the lifetimes of both emissions; R-lines and low energy sidebands. This is clearly observed

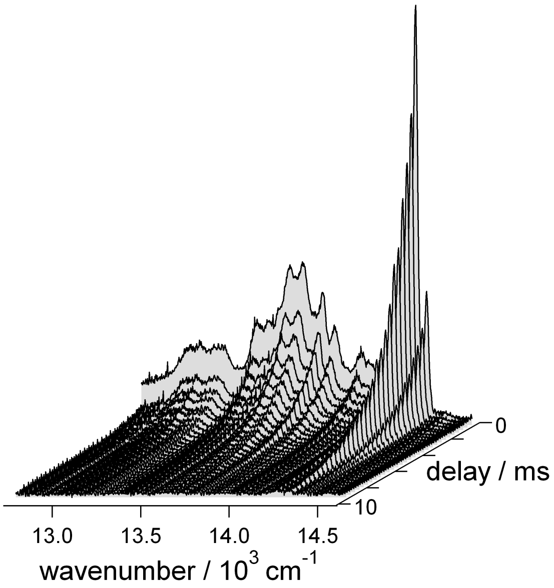

Figure 5.58: 25 K time-resolved luminescence of GGG: 0.5%Cr^{3+} upon pulsed excitation at 21980 cm^{-1} using different delay times after the excitation pulse. (Experimental details in Section 4.3.3).

in the 25 K time-resolved luminescence spectra depicted in Fig. 5.58 which shows both R-line luminescence at around 14410 cm^{-1}, and sidebands emission centered at 19500 cm^{-1}, upon excitation at 21980 cm^{-1}, obtained at different delay times after the excitation pulse. On the basis of this temporal behavior, the existence of different Cr^{3+} sites as well as Cr^{3+} pairs luminescence can be rejected.

Figure 5.59 shows the temperature dependence of the Cr^{3+} luminescence lifetime in GGG: Cr^{3+} nanocrystals. The same lifetime is expected for the emission from the R-line region and from the sidebands if the $^4T_2$ state is thermally populated, or if both ^2E and $^4T_2$ states are coupled through spin-orbit interaction [66], [69]. However, the thermal coupling model cannot account for changes in lifetime when one of the states is completely depopulated, which is the case of low temperature data [65]. A model including spin-orbit coupling of the excited states leads to a common lifetime dominated by the magnitude of the zero phonon line (ZPL) energy separation between the ^2E and $^4T_2$ states, $\Delta E = E_{\mathrm{ZPL}}(^4T_2) - E_{\mathrm{ZPL}}(^2E) = 490$ cm^{-1}. This value is a little higher than the previously reported for the bulk, 300-400 cm^{-1} [69], [70]. The mixed states resulting from the spin-orbit interaction are given by:

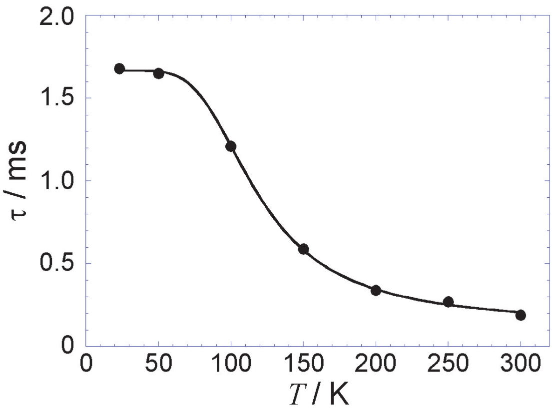

Figure 5.59: Temperature dependence of the Cr^{3+} emission lifetime in GGG: Cr^{3+} nanoparticles. The line corresponds to the least-square fitting to eq. 5.9 (see text).

$$\Psi_1 = c|^2E\rangle + d|^4T_2\rangle \tag{5.6}$$

$$\Psi_2 = d|^2E\rangle - c|^4T_2\rangle \tag{5.7}$$

being the spin-orbit mixing coefficients, c and d:

$$\begin{aligned} c &= \sqrt{\frac{1}{2}}\left(1+\frac{\Delta E}{\Delta E_{SO}}\right)^{\frac{1}{2}} \\ d &= \sqrt{\frac{1}{2}}\left(1-\frac{\Delta E}{\Delta E_{SO}}\right)^{\frac{1}{2}} \end{aligned} \tag{5.8}$$

with $\Delta E_{\mathrm{SO}} = \sqrt{\Delta E^2 + 4V_{\mathrm{SO}}^2}$, and V_{SO} being the spin-orbit interaction energy.

Considering the lifetimes of each state, τ_1 and τ_2, the common lifetime can be described as [51], [65]:

$$\frac{1}{\tau} = \frac{\frac{1}{\tau_1} + 3\frac{1}{\tau_2}\exp\left(\frac{-\Delta E_{\mathrm{SO}}}{kT}\right)}{1 + 3\exp\left(\frac{-\Delta E_{\mathrm{SO}}}{kT}\right)} \tag{5.9}$$

with

$$\begin{aligned} \frac{1}{\tau_1} &= c^2\frac{1}{\tau_E} + d^2\frac{1}{\tau_T} \\ \frac{1}{\tau_2} &= d^2\frac{1}{\tau_E} + c^2\frac{1}{\tau_T} \end{aligned} \tag{5.10}$$

where τ_E and τ_T are the intrinsic decays of the ^2E and $^4T_2$ levels, respectively.

The obtained fitting parameters are $V_{\mathrm{SO}} = 58$ cm^{-1}, $\tau_1 = 1.67$ ms and $\tau_2 = 80$ μs. The spin-orbit interaction is reduced in comparison with the typical free ion value, 215 cm^{-1}, as a consequence of the dynamic Jahn-Teller effect, which is known as the Ham effect [75], [76]. Since the $^4T_2 \rightarrow {}^4A_2$ transition is spin-allowed with a short lifetime, whereas the $^2E \rightarrow {}^4A_2$ one is spin-forbidden with a long lifetime, the lifetime at low temperature, which corresponds to τ_1, represents the maximum contribution of the ^2E state observed in the 25-300 K temperature range; however it cannot be assumed that τ_1 is the intrinsic ^2E lifetime. The observed thermal quenching of the lifetime is due to thermal activation of the $^4T_2$ energy level contribution.

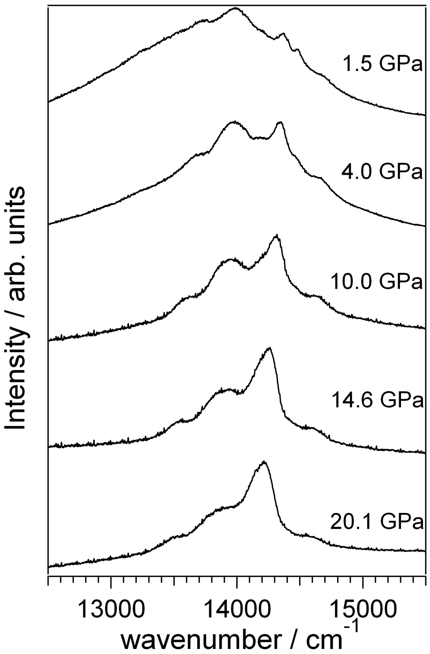

Figure 5.60: Pressure dependence of the GGG: 0.5%Cr^{3+} nanocrystals RT luminescence upon excitation at 21980 cm^{-1}.

- **High pressure effect.**

RT emission spectra in GGG: 0.5%Cr^{3+} upon excitation at 21980 cm^{-1} for various pressures up to 20 GPa are shown in Fig. 5.60. At 1.5 GPa, the broadband luminescence from the $^4T_2$ Cr^{3+} state with a small ^2E emission contribution is observed. When pressure is raised the emission changes, and above 15 GPa the band

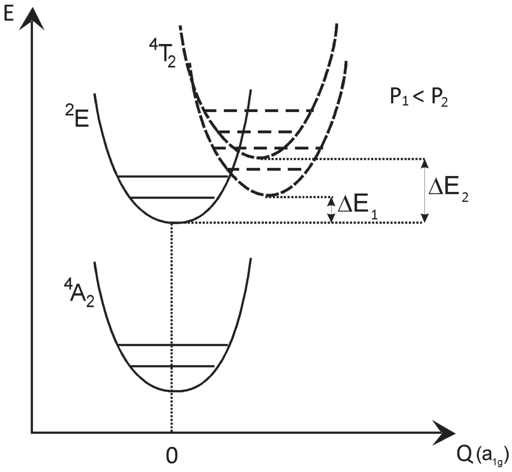

Figure 5.61: Schematic representation of the configurational coordinate curves in harmonic approximation, Q(a_{1g}), for the $^4T_2$ and ^2E Cr^{3+} emitting states at different pressures.

due to $^2E \rightarrow {}^4A_2$ Cr^{3+} emission is predominant. Nevertheless, a structured narrow R-line emission is not obtained for GGG: 0.5%Cr^{3+} nanoparticles at RT even at pressures as high as 20 GPa. In this sense, the pressure-induced changes in GGG: Cr^{3+} nanoparticles correspond neither with the results obtained for the bulk [69], nor with the temperature dependence of the Cr^{3+} luminescence described in the previous section. A slight red-shift with pressure is observed for the ruby-like emission. The effect of pressure on the $^4T_2$ and ^2E states can be described considering that the $^4T_2$ energy depends linearly on the crystal-field splitting, Δ, while the ^2E state is weakly coupled to the lattice. When pressure increases, the volume of the CrO_6 octahedron decreases, and therefore the bond distances $R_{\text{Cr-O}}$ decrease; since $\Delta \propto 1/R^5$, the $^4T_2$ energy increases. On the contrary, the ^2E energy is only weakly affected by pressure by the small decrease of B [51]. This fact leads to an important increment of the energy difference between both states, ΔE, with pressure (Fig. 5.61), and to a consequent decrease in the contribution of the $^4T_2$ state to the mixed emitting state Ψ_1, reflected in the reduction of the d mixing coefficient. As a result, the spin-allowed character of the emission is reduced. Besides, the thermal population of the $^4T_2$ state is also reduced due to the increase of ΔE upon increasing pressure.

The pressure dependence of the emission lifetimes in GGG: 0.5%Cr^{3+} nanocrystals has been measured at two different zones centered at 14410 cm^{-1} and 13985 cm^{-1}, after pulsed excitation at 21980 cm^{-1}, and the best exponential fittings are collected in Table 5.9. The fact that the same lifetimes have been measured at both energies reflects again the coupling between the $^4T_2$ and ^2E states. The Cr^{3+} emission evolution when pressures increases, from a broadband $^4T_2 \rightarrow {}^4A_2$ luminescence to a ruby-like $^2E \rightarrow {}^4A_2$ emission, is accompanied, as expected, by an increase in the emission lifetime. Similar behavior although with longer lifetimes was observed for the bulk in Ref. [69]. The reduction of both the thermal population of the $^4T_2$ state, and the ^2E-$^4T_2$ spin orbit mixing contribute to the emission lifetime increase with pressure.

Table 5.9: Lifetimes of the GGG: 0.5%Cr^{3+} nanocrystals emission in the 1.5-20 GPa range.

P / GPa	τ/ms (14410 cm^{-1})	τ/ms (13985 cm^{-1})
1.0	0.24 ± 0.02	0.22 ± 0.02
1.5	0.24 ± 0.02	0.25 ± 0.02
4.0	0.45 ± 0.05	0.40 ± 0.06
7.6	1.03 ± 0.07	0.96 ± 0.03
10.0	1.87 ± 0.06	1.79 ± 0.04
14.6	3.00 ± 0.08	
20.1	3.40 ± 0.10	

Since the energy separation between both states, ΔE, increases with pressure (see Fig. 5.61), it is possible to model the dependence of lifetime on pressure assuming a linear pressure dependence: $\Delta E_{\mathrm{P}} = \Delta E + \alpha P$. Figure 5.62 shows the pressure dependence of the Cr^{3+} emission lifetime in GGG: Cr^{3+} nanoparticles as well as the fitting to eq. 5.9. The resultant fitting values are $\alpha = 74$ cm^{-1}/GPa, $\tau_1 = 3.51$ ms and $\tau_2 = 29.5$ μs. The fitted shift rate is consistent with the experimental values observed in bulk GGG: Cr^{3+} ($\alpha = 106$ cm^{-1}/GPa) [69], and in Cr^{3+}-doped LiCaAlF$_6$ ($\alpha = 86$ cm^{-1}/GPa) [67]. Since a steady-state lifetime seems to be reached in Fig. 5.62 at 20 GPa, τ_1 and τ_2 are an accurate estimation for the lifetimes of the ^2E and $^4T_2$ states, respectively. The fact that the τ_2 value is significantly smaller than the pure $^4T_2$ lifetime previously reported for bulk GGG: Cr^{3+} (65 μs) and YAG: Cr^{3+} (136 μs) is remarkable [69].

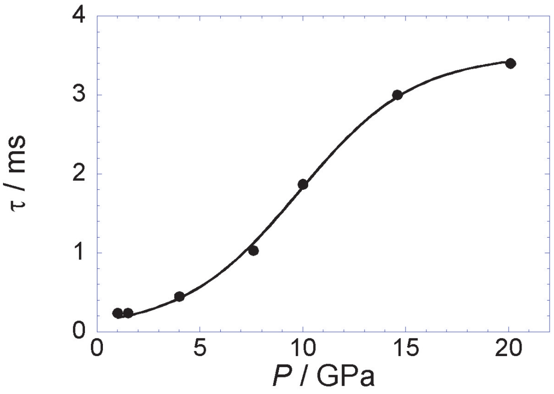

Figure 5.62: Pressure dependence of the Cr^{3+} luminescence lifetime in GGG: Cr^{3+} nanocrystals. The line corresponds to the least-square fitting to eq. 5.9 (see text).

Conclusions

A study on the temperature and pressure dependence of the luminescence and lifetime properties of Cr^{3+}-doped GGG nanoparticles (30 nm in size) has been carried out. A spectral transformation from broadband, $^4T_2 \rightarrow {}^4A_2$, to narrowband, $^2E \rightarrow {}^4A_2$ emission, along with an increase in the lifetime is measured for GGG nanoparticles at low temperatures. This behavior with temperature is analogous to the pressure dependence observed in GGG: Cr^{3+} bulk and it indicates that low temperature may have the same tuning effects on nanoparticles as high pressure in the bulk. On the contrary, the influence of high pressure on GGG: Cr^{3+} nanoparticles luminescence is slightly different. A change from Cr^{3+} broadband to ruby-like emission is also detected, but at RT structured R-line emission is not obtained even at 20 GPa. The lifetime dependence on temperature and pressure has been modeled considering the spin-orbit coupling between the $^4T_2$ and ^2E Cr^{3+} states.

Bibliography

[1] S. Heer, K. Kömpe, H.U. Güdel, and M. Haase. Highly Efficient Multicolor Upconversion Emission in Transparent Colloids of Lanthanide-Doped $NaYF_4$ Nanocrystals. *Adv. Mater.*, **16**: 2102–2105, 2004.

[2] K.W. Krämer, D. Biner, G. Frei, H.U. Güdel, M.P. Hehlen, and S.R. Lüthi. Hexagonal Sodium Yttrium Fluoride Based Green and Blue Emitting Upconversion Phosphors. *Chem. Mater.*, **16**: 1244–1251, 2004.

[3] M.F. Joubert. Photon avalanche upconversion in rare earth laser materials. *Opt. Mater.*, **11**: 181–203, 1999.

[4] E. Heumann, S. Bär, K. Rademaker, G. Huber, S. Butterworth, A. Diening, and W. Seelert. Semiconductor-laser-pumped high-power upconversion laser. *Appl. Phys. Lett.*, **88**: 061108, 2006.

[5] S. Sivakumar, P.R. Diamente, and F.C.J.M. van Veggel. Silica-Coated Ln^{3+}-Doped LaF_3 Nanoparticles as Robust Down- and Upconverting Biolabels. *Chem.-A Eur. J.*, **12**: 5878–5884, 2006.

[6] M. Nyk, R. Kumar, T.Y. Ohulchanskyy, E.J. Bergey, and P.N. Prasad. High Contrast in Vitro and in Vivo Photoluminescence Bioimaging Using Near Infrared to Near Infrared Up-Conversion in Tm^{3+} and Yb^{3+} Doped Fluoride Nanophosphors. *Nano Lett.*, **8**: 3834–3838, 2008.

[7] T. Trupke, A. Shalav, B.S. Richards, P. Würfel, and M.A. Green. Efficiency enhancement of solar cells by luminescent up-conversion of sunlight. *Solar Energy Mater. Solar Cells*, **90**: 3327–3338, 2006.

[8] M. Bruchez Jr, M. Moronne, P. Gin, S. Weiss, and A.P. Alivisatos. Semiconductor Nanocrystals as Fluorescent Biological Labels. *Science*, **281**: 2013–2016, 1998.

[9] J.C. Boyer, F. Vetrone, J.A. Capobianco, A. Speghini, and M. Bettinelli. Yb^{3+} ion as a sensitizer for the upconversion luminescence in nanocrystalline $Gd_3Ga_5O_{12}$:Ho^{3+}. *Chem. Phys. Lett.*, **390**: 403–407, 2004.

[10] F.W. Ostermayer and L.G. Van Uitert. Cooperative Energy Transfer from Yb^{3+} to Tb^{3+} in YF_3. *Phys. Rev. B*, **1**: 4208–4212, 1970.

[11] R.S. Brown, W.S. Brocklesby, W.L. Barnes, and J.E. Townsend. Cooperative energy transfer in silica fibres doped with ytterbium and terbium. *J. Lumin.*, **63**: 1–7, 1995.

[12] G.M. Salley, R. Valiente, and H.U. Güdel. Cooperative Yb^{3+}-Tb^{3+} dimer excitations and upconversion in $Cs_3Tb_2Br_9$: Yb^{3+}. *Phys. Rev. B*, **67**: 134111, 2003.

[13] W. Strek, P.J. Dereń, A. Bednarkiewicz, Y. Kalisky, and P. Boulanger. Efficient upconversion in $KYb_{0.8}Eu_{0.2}(WO_4)_2$ crystal. *J. Alloys Compounds*, **300-301**: 180–183, 2000.

[14] G.S. Maciel, A. Biswas, and P.N. Prasad. Infrared-to-visible Eu^{3+} energy upconversion due to cooperative energy transfer from an Yb^{3+} ion pair in a sol-gel processed multi-component silica glass. *Opt. Commun.*, **178**: 65–69, 2000.

[15] R.W.G. Wyckoff, editor. *Crystal Structures*, volume 2. John Wiley and Sons, New York, London, 1963.

[16] M. Mandel. Paramagnetic Resonance of Yb^{3+} in Yttrium Oxide. *Appl. Phys. Lett.*, **2**: 197–198, 1963.

[17] J.A. Capobianco, F. Vetrone, J.C. Boyer, A. Speghini, and M. Bettinelli. Enhancement of Red Emission via Upconversion in Bulk and Nanocrystalline Cubic Y_2O_3: Er^{3+}. *J. Phys. Chem. B*, **106**: 1181–1187, 2002.

[18] R. Buisson and J.C. Vial. Transfer inside pairs of Pr^{3+} in LaF_3 studied by upconversion fluorescence. *J. Phys. (France) Lett.*, **42**: 115–118, 1981.

[19] R. Valiente, O.S. Wenger, and H.U. Güdel. Upconversion luminescence in Yb^{3+} doped $CsMnCl_3$: Spectroscopy, dynamics, and mechanisms. *J. Chem. Phys.*, **116**: 5196–5204, 2002.

[20] J.F. Suyver, J. Grimm, M.K. van Veen, D. Biner, K.W. Krämer, and H.U. Güdel. Upconversion spectroscopy and properties of $NaYF_4$ doped with Er^{3+}, Tm^{3+} and/or Yb^{3+}. *J. Lumin.*, **117**: 1–12, 2006.

[21] A. Aebischer, M. Hostettler, J. Hauser, K. Krämer, T. Weber, H.U. Güdel, and H.B. Bürgi. Structural and Spectroscopic Characterization of Active Sites in a Family of Light-Emitting Sodium Lanthanide Tetrafluorides. *Angew. Chem. Int. Ed.*, **45**: 2802–2806, 2006.

[22] P. Boutinaud, R. Mahiou, N. Martin, and M. Malinowski. Luminescence from Pr^{3+} $^3P_1$ and $^3P_2$ states in β-$NaYF_4$: Pr^{3+}. *J. Lumin.*, **72-74**: 809–811, 1997.

[23] C.C. Koch. Synthesis of nanostructured materials by mechanical milling: Problems and oportunities. *Nanostruct. Mater.*, **9**: 13–22, 1997.

[24] M. Pollnau, D.R. Gamelin, S.R. Lüthi, H.U. Güdel, and M.P. Hehlen. Power dependence of upconversion luminescence in lanthanide and transition-metal-ion systems. *Phys. Rev. B*, **61**: 3337–3346, 2000.

[25] J.F. Suyver, A. Aebischer, S. García-Revilla, P. Gerner, and H.U. Güdel. Anomalous power dependence of sensitized upconversion luminescence. *Phys. Rev. B*, **71**: 125123, 2005.

[26] J.C. Boyer, F. Vetrone, J.A. Capobianco, A. Speghini, M. Zambelli, and M. Bettinelli. Investigation of the upconversion processes in nanocrystalline $Gd_3Ga_5O_{12}$: Ho^{3+}. *J. Lumin.*, **106**: 263–268, 2004.

[27] M. Daldosso, D. Falcomer, A. Speghini, M. Bettinelli, S. Enzo, B.Lasio, and S. Polizzi. Synthesis, structural investigation and luminescence spectroscopy of nanocrystalline $Gd_3Ga_5O_{12}$ doped with lanthanide ions. *J. Alloys Compounds*, **451**: 553–556, 2008.

[28] M. Pang and J. Lin. Growth and optical properties of nanocrystalline $Gd_3Ga_5O_{12}$: Ln (Ln= Eu^{3+}, Tb^{3+}, Er^{3+}) powders and thin films via Pechini sol-gel process. *J. Cryst. Growth*, **284**: 262–269, 2005.

[29] M. Daldosso, D. Falcomer, A. Speghini, P. Ghigna, and M. Bettinelli. Synthesis, EXAFS investigation and optical spectroscopy of nanocrystalline $Gd_3Ga_5O_{12}$ doped with Ln^{3+} ions (Ln=Eu, Pr). *Opt. Mat.*, **30**: 1162–1167, 2008.

[30] B. Keszei, J. Paitz, J. Vandlik, and A. Süveges. Control of Nd and Cr concentrations in Nd, Cr: $Gd_3Ga_5O_{12}$ single crystals grown by Czochralski method. *J. Cryst. Growth*, **226**: 95–100, 2001.

[31] P. Dorenbos. The $4f^n \leftrightarrow 4f^{n-1}5d$ transitions of the trivalent lanthanides in halogenides and chalcogenides. *J. Lumin.*, **91**: 91–106, 2000.

[32] G. Blasse and A. Bril. *Philips Res. Repts*, **22**: 481, 1967.

[33] A. Meijerink, R. Wegh, P. Vergeer, and T. Vlugt. Photon management with lanthanides. *Opt. Mater.*, **28**: 575581, 2006.

[34] B. Lai, J. Wang, and Q. Su. Ultraviolet and visible upconversion emission in Tb^{3+}/Yb^{3+} co-doped fluorophosphate glasses. *Appl. Phys. B*, **98**: 4147, 2010.

[35] H. Liang, G. Chen, L. Li, Y. Liu, F. Qin, and Z. Zhang. Upconversion luminescence in Tb^{3+}/Yb^{3+}-codoped monodisperse $NaYF_4$ nanocrystals. *Opt. Commun.*, **282**: 3028–3031, 2009.

[36] S. Sivakumar and F.C.J.M. van Veggel. Red, Green, and Blue Light Through Cooperative Up-Conversion in Sol-Gel Thin Films Made with $Yb_{0.80}La_{0.15}Tb_{0.05}F_3$ and $Yb_{0.80}La_{0.15}Eu_{0.05}F_3$ Nanoparticles. *J. Disp. Technol.*, **3**: 176–183, 2007.

[37] W.F. van der Weg, Th.J.A. Popma, and A.T. Vink. Concentration dependence of UV and electron-excited Tb^{3+} luminescence in $Y_3Al_5O_{12}$. *J. Appl. Phys.*, **57**: 5450–5456, 1985.

[38] H. Wang, C. Duan, and P.A. Tanner. Visible Upconversion Luminescence from Y_2O_3: Eu^{3+}, Yb^{3+}. *J. Phys. Chem. C*, **112**: 16651–16654, 2008.

[39] F.S. Liu, Q.L. Liu, J.K. Liang, J. Luo, L.T. Yang, G.B. Song, Y. Zhang, L.X. Wang, J.N. Yao, and G.H. Rao. Crystal structure and photoluminescence of Tb^{3+} doped Y_3GaO_6. *J. Alloys Compd.*, **425**: 278–283, 2006.

[40] Y.P. Naik, M. Mohapatra, N.D. Dahale, T.K. Seshagiri, V. Natarajan, and S.V. Godbole. Synthesis and luminescence investigation of RE^{3+} (Eu^{3+}, Tb^{3+} and Ce^{3+})-doped lithium silicate (Li_2SiO_3). *J. Lumin.*, **129**: 1225–1229, 2009.

[41] X. Liu, X. Wang, and Z. Wang. Selectively excited emission and Tb^{3+}-Ce^{3+} energy transfer in yttrium aluminum garnet. *Phys. Rev. B*, **39**: 10633–10639, 1989.

[42] R.S. Meltzer, S.P. Feofilov, B. Tissue, and H.B. Yuan. Dependence of fluorescence lifetimes of Y_2O_3: Eu^{3+} nanoparticles on the surrounding medium. *Phys. Rev. B*, **60**: R14012–R14015, 1999.

[43] A. Speghini, M. Bettinelli, P. Riello, S. Bucella, and A. Benedetti. Preparation, structural characterization, and luminescence properties of Eu^{3+}-doped nanocrystalline ZrO_2. *J. Mater. Res.*, **20**: 2780–2791, 2005.

[44] G.M. Salley, R. Valiente, and H.U. Güdel. Phonon-assisted cooperative sensitization of Tb^{3+} in $SrCl_2$: Yb, Tb. *J. Phys.: Condens. Matter*, **14**: 5461–5475, 2002.

[45] K. Krämer and H.U. Güdel. Upconversion luminescence in K_2LaX_5: Er^{3+} ($X = Cl$, Br). *J. Alloy. Compd.*, **207-208**: 128–132, 1994.

[46] O.S. Wenger, G.M. Salley, R. Valiente, and H.U. Güdel. Luminescence upconversion under hydrostatic pressure in the 3d-metal systems Ti^{2+}: NaCl and Ni^{2+}: $CsCdCl_3$. *Phys. Rev. B*, **65**: 212108, 2002.

[47] R. Valiente, O.S. Wenger, and H.U. Güdel. New photon upconversion processes in Yb^{3+} doped $CsMnCl_3$ and $RbMnCl_3$. *Chem. Phys. Lett.*, **320**: 639–644, 2000.

[48] S. Heer, M. Wermuth, K. Krämer, and H.U. Güdel. Sharp ^{2}E upconversion luminescence of Cr^{3+} in $Y_3Ga_5O_{12}$ codoped with Cr^{3+} and Yb^{3+}. *Phys. Rev. B*, **65**: 125112, 2002.

[49] R. Valiente, O.S. Wenger, and H.U. Güdel. Near-infrared-to-visible photon upconversion process induced by exchange interactions in Yb^{3+}-doped $RbMnCl_3$. *Phys. Rev. B*, **63**: 165102, 2001.

[50] P. Gerner, O.S. Wenger, R. Valiente, and H.U. Güdel. Green and Red Light Emission by Upconversion from the near-IR in Yb^{3+} Doped $CsMnBr_3$. *Inorg. Chem.*, **40**: 4534, 2001.

[51] B. Henderson and G.F. Imbusch, editors. *Optical Spectroscopy of Inorganic Solids.* Clarendon Press, Oxford, 1989.

[52] S.C. Abrahams, P. Marsh, and C.D. Brandle. Laser and phosphor host $La_{1-x}MgAl_{11+x}O_{19}$ ($x = 0.050$): Crystal structure at 295 K. *J. Chem. Phys.*, **86**: 4221–4227, 1987.

[53] S. Nukuta and T. Onimaru. Patent 7.037.445. 2006.

[54] V. Adelskold. X-ray studies on magneto-plumbite and other substances resembling beta-alumina. *Arkiv. Kemi Mineral. Geol. A 12*, **29**: 1–9, 1938.

[55] N. Iyi, Z. Inoue, S. Takekawa, and S. Kimura. The crystal structure of lanthanum hexaaluminate. *J. Solid State Chem.*, **54**: 70–77, 1984.

[56] M. Gasperin, M.C. Saine, A. Kahn, F. Laville, and M. Lejus. Influence of M^{2+} Ions Substitution on the Structure of Lanthanum Hexaaluminates with Magnetoplumbite Structure. *J. Solid State Chem.*, **54**: 61–69, 1984.

[57] E. Nakazawa and S. Shionoya. Cooperative Luminescence in $YbPO_4$. *Phys. Rev. Lett.*, **25**: 1710–1712, 1970.

[58] M.P. Hehlen and H.U. Güdel. Optical spectroscopy of the dimer system $Cs_3Yb_2Br_9$. *J. Chem. Phys.*, **98**: 1768–1775, 1993.

[59] R.T. Wegh and A. Meijerink. Cooperative luminescence of ytterbium(III) in La_2O_3. *Chem. Phys. Lett.*, **246**: 495–498, 1995.

[60] P. Goldner, F. Pellé, D. Meichenin, and F. Auzel. Cooperative luminescence in ytterbium-doped $CsCdBr_3$. *J. Lumin.*, **71**: 137–150, 1997.

[61] M.N. Sanz-Ortiz and F. Rodríguez. Photoluminescence properties of Jahn-Teller transition-metal ions. *J. Chem. Phys.*, **131**: 124512, 2009.

[62] N.F. Mott. *Proc. Roy. Soc. (London)*, **A 167**: 384, 1938.

[63] J. Luzón, J. Campo, F. Palacio, G.J. McIntyre, and A. Millán. Understanding magnetic interactions in the series $A_2FeX_5 \cdot H_2O$ (A=K, Rb; X=Cl, Br). I. Spin densities by polarized neutron diffraction and DFT calculations. *Phys. Rev. B*, **78**: 054414, 2008.

[64] M.P. Hehlen, A. Kuditcher, S.C. Rand, and S.R. Lüthi. Site-Selective, Intrinsically Bistable Luminescence of Yb^{3+} Ion Pairs in $CsCdBr_3$. *Phys. Rev. Lett.*, **82**: 3050–3053, 1999.

[65] K.L. Bray, editor. *High pressure probes of electronic structure and luminescence properties of transition metal and lanthanides systems*, volume 213 of *Topic in Current Chemistry.* Spring-Verlag, Berlin, 2001.

[66] W.A. Wall, J.T. Karpick, and B. Di Bartolo. Temperature dependence of the vibronic spectrum and fluorescence lifetime of YAG: Cr^{3+}. *J. Phys. C: Solid St. Phys.*, **4**: 3258–3264, 1971.

[67] M.N. Sanz-Ortiz, F. Rodríguez, I. Hernández, R. Valiente, and S. Kück. Origin of the ^2E - $^4T_2$ Fano resonance in Cr^{3+}-doped $LiCaAlF_6$: Pressure-induced excited-state crossover. *Phys. Rev. B*, **81**: 045114, 2010.

[68] Y.R. Shen and K.L. Bray. Effect of pressure and temperature on the lifetime of Cr^{3+} in yttrium aluminum garnet. *Phys. Rev. B*, **56**: 10882–10891, 1997.

[69] U. Hömmerich and K.L. Bray. High-pressure laser spectroscopy of Cr^{3+}: $Gd_3Sc_2Ga_3O_{12}$ and Cr^{3+}: $Gd_3Ga_5O_{12}$. *Phys. Rev. B*, **51**: 12133–12141, 1995.

[70] F.M. Hashmi, R.C. Powell, and G. Boulon. Energy transfer and radiationless relaxation processes in Nd^{3+} and Cr^{3+} doped mixed garnet crystals. *Opt. Mat.*, **1**: 281–298, 1992.

[71] J.F. Dolan, L.A. Kappers, and R.H. Bartram. Pressure and temperature dependence of chromium photoluminescence in K_2NaGaF_6: Cr^{3+}. *Phys. Rev. B*, **33**: 7339–7341, 1986.

[72] S. Heer, M. Wermuth, K. Krämer, D. Ehrentraut, and H.U. Güdel. Up-conversion excitation of sharp Cr^{3+} ^2E emission in YGG and YAG codoped with Cr^{3+} and Yb^{3+}. *J. Lumin.*, **94-95**: 337–341, 2001.

[73] E.V Zharikov, S.V Lavrishchev, V.V Laptev, V.G Ostroumov, Z.S. Saidov, V.A. Smirnov, and I.A Shcherbakov. New possibilities for Cr^{3+} ions as activators of the active media of solid-state lasers. *Sov. J. Quantum Electron.*, **14**: 332–336, 1984.

[74] B. Di Bartolo, editor. *27th Workshop: Luminescence of Inorganic Materials and Bioimaging: Metal-to-Metal Energy and Electron Transfer*. Erice, Sicily, Italy, 22-28 June 2010.

[75] J.S. Griffith, editor. *The Theory of Transition-Metal Ions*. Cambridge University Press, London, 1971.

[76] F.S. Ham. Dynamical Jahn-Teller Effect in Paramagnetic Resonance Spectra: Orbital Reduction Factors and Partial Quenching of Spin-Orbit Interaction. *Phys. Rev.*, **138**: A1727–A1740, 1965.